AGU PUBLICATIONS

JGR

Journal of Geophysical Research: Space Physics

RESEARCH ARTICLE
10.1002/2016JA023237

Special Section:
Geospace system responses to the St. Patrick's Day storms in 2013 and 2015

Key Points:
- Storm had excellent ground/space data coverage, allowing evaluation of relations between major storm phenomena often considered separately
- Identified three southward IMF electric fields driving modes that were reflected in the aurora and ionospheric and field-aligned currents
- The third mode was extremely bursty, giving common driving of auroral and current structures, TEC changes, and ring current injection

Correspondence to:
L. R. Lyons,
larry@atmos.ucla.edu

Citation:
Lyons, L. R., et al. (2016), The 17 March 2013 storm: Synergy of observations related to electric field modes and their ionospheric and magnetospheric Effects, *J. Geophys. Res. Space Physics*, *121*, 10,880–10,897, doi:10.1002/2016JA023237.

Received 26 JUL 2016
Accepted 9 OCT 2016
Accepted article online 12 OCT 2016
Published online 11 NOV 2016

The 17 March 2013 storm: Synergy of observations related to electric field modes and their ionospheric and magnetospheric Effects

L. R. Lyons[1], B. Gallardo-Lacourt[1], S. Zou[2], J. M. Weygand[3], Y. Nishimura[1], W. Li[1], M. Gkioulidou[4], V. Angelopoulos[3], E. F. Donovan[5], J. M. Ruohoniemi[6], B. J. Anderson[4], S. G. Shepherd[7], and N. Nishitani[8]

[1]Department of Atmospheric and Oceanic Sciences, University of California, Los Angeles, California, USA, [2]Climate and Space Sciences and Engineering Department, University of Michigan, Ann Arbor, Michigan, USA, [3]Department of Earth, Planetary, and Space Sciences, University of California, Los Angeles, California, USA, [4]Applied Physics Laboratory, Johns Hopkins University, Laurel, Maryland, USA, [5]Department of Physics and Astronomy, University of Calgary, Calgary, Alberta, Canada, [6]Bradley Department of Electrical and Computer Engineering, Virginia Tech, Blacksburg, Virginia, USA, [7]Thayer School of Engineering, Dartmouth College, Hanover, New Hampshire, USA, [8]Solar-Terrestrial Environment Laboratory, Nagoya University, Nagoya, Japan

Abstract The main phase of the 17 March 2013 storm had excellent coverage from ground-based instruments and from low- and high-altitude spacecraft, allowing for evaluation of the relations between major storm time phenomena that are often considered separately. The shock impact with its concurrent southward interplanetary magnetic field (IMF) immediately drove dramatic poleward expansion of the poleward boundary of the auroral oval (implying strong nightside reconnection), strong auroral activity, and strong penetrating midlatitude convection and ionospheric currents. This was followed by periods of southward IMF driving of electric fields that were at first relatively smooth as often employed in storm modeling but then became extremely bursty and structured associated with equatorward extending auroral streamers. The auroral oval did not expand much further poleward during these two latter periods, suggesting a lower overall nightside reconnection rate than that during the first period and approximate balance with dayside reconnection. Characteristics of these three modes of driving were reflected in horizontal and field-aligned currents. Equatorward expansion of the auroral oval occurred predominantly during the structured convection mode, when electric fields became extremely bursty. The period of this third mode also approximately corresponded to the time of largest equatorward motion of the ionospheric trough, of apparent transport of high total electron content (TEC) features into the auroral oval from the polar cap, and of largest earthward injection of ions and electrons into the ring current. The enhanced responses of the aurora, currents, TEC, and the ring current indicate a common driving of all these storm time features during the bursty convection mode period.

1. Introduction

An essential feature of magnetic storms is the spatial extension of the disturbance convection, ionospheric currents, and particle precipitation to middle and low latitudes during the main phase. The features of interest here are the earthward penetration of the plasma sheet in the magnetotail (equatorward in the ionosphere); the equatorward expansion of the auroral oval, of oval-related ionospheric currents, and of the region 2 (R2) field-aligned current (FAC) system; the equatorward motion of the poleward edge of midlatitude ionospheric trough; the injection of particles to form the storm time ring current; and ionospheric density enhancements that move throughout the nightside auroral oval. Generally, these signatures are treated separately even though they share underlying physical processes. However, the richness of the extensive array of overlapping data sets for the 17 March 2013 storm gives us the opportunity to identify relationships between these disparate features and place their development in the context of a common dynamical origin.

The 17 March 2013 storm is a coronal mass ejection-driven event with a shock that impacted the magnetosphere at 06:00 UT [*Baker et al.*, 2014], and there has been much interest in ring current particle injections [e.g., *Gkioulidou et al.*, 2014] and radiation belt electrons [e.g., *Hudson et al.*, 2015; *Li et al.*, 2014, 2015] for this event (the storm time radiation belt electron enhancement occurred after the period of interest here).

During the main phase of this storm, we have excellent and overlapping coverage of the aurora from the array of Time History of Events and Macroscale Interactions during Substorms (THEMIS) ground-based all-sky imagers (ASIs) [*Mende et al*., 2008], of ionospheric flows from the ground-based Super Dual Auroral Radar Network (SuperDARN) and the Poker Flat Incoherent Scatter Radar (PFISR), of the global distribution of magnetic field-aligned currents (FACs) from the Active Magnetosphere and Planetary Electrodynamics Response Experiment (AMPERE; http://ampere.jhuapl.edu/index.html) [*Anderson et al*., 2014], and of in situ plasma sheet particles from the two Van Allen Probes (VAP A and B) [*Mauk et al*., 2013] and the THEMIS probes near the equatorial plane [*Angelopoulos*, 2008]. In addition to these, we also have the routinely available maps of vertical total electron content (TEC) from the Madrigal database [*Rideout and Coster*, 2006]; magnetic fields from ground-based magnetometers; and particle measurements from the low-altitude, polar-orbiting, Defense Meteorological Satellite Program (DMSP) spacecraft. Here we use these data to explore the possible common driving by midlatitude electric fields of the penetration of the plasma sheet, auroral oval, and its ionospheric currents and of the R2 currents, major ionospheric density features, and the formation of the storm time ring current. We find the existence of different modes of midlatitude electric fields and currents during the main phase of this storm and present evidence for which of the three modes is the most important for the driving of the above storm time phenomena.

2. Radar and ASI Observations

Figure 1 shows, from top to bottom, the Wind solar wind dynamic pressure P_{dyn}; the OMNI interplanetary magnetic field (IMF) as propagated to the dayside magnetopause; the SuperMAG [*Gjerloev*, 2012] ground magnetometer upper *U* and lower *L* auroral magnetic indices; the SuperMAG ring current index for all magnetic local time (MLT) and within the dusk, noon, dawn, and midnight sectors; and ground magnetometer observations from North American stations near 66–67° magnetic latitude with increasing UT of midnight (indicated by small vertical arrows). These SuperMAG indices are based on the traditional *AU*, *AL*, and *SYM-H* indices, but with many more, and well-distributed stations. The OMNI IMF data are shown further shifted by ~10 min so that the shock impact time agrees with the 06:00 UT impact time seen by the dayside ground magnetometers. The Wind P_{dyn} is shown because of data gaps in the OMNI P_{dyn} around the time of the shock. It is further shifted by ~30 min relative to the IMF data to agree with the time of shock impact and shows the large increase in P_{dyn} of the shock that impacted the magnetosphere. Maroon-colored dashed boxes identify the four main periods (periods 1–4) of southward IMF that were seen after the shock arrival and during the storm main phase, each being reflected in the auroral *L* index.

During the main phase period shown, the ring current index for all MLT decreased to −110 nT, making this a moderate intensity storm. The individual magnetometer stations in Figure 1 show numerous fluctuations of the N (northward) component; however, only one decrease was associated with a substorm that could be identified in the auroral observations. Some decreases were clearly associated with the major southward turnings of the IMF, while most of the others do not correlate well between stations and were most likely associated with the longitudinally localized auroral streamers and flow bursts that are discussed later and seen in subsequent figures. Because of the localized nature of flow bursts, and the inclusion of substantially more magnetometer stations, the auroral *L* index is relatively smooth.

2.1. Postshock Southward IMF Period 1 (06:00–06:16 UT)

Movie S1 shows auroral images overlaid with line-of-sight (LOS) flow velocities from the SuperDARN radars from 05:40 to 13:00 UT, which includes the shock impact and the storm main phase development. Plots are shown every 30 s and include mergers of the images from all available ASIs over Canada and Alaska and, from west to east, LOS flow velocities from the midlatitude Christmas Valley west and east (CVW and CVE) and the Fort Hays west and east (FHW and FHE) radars (data taken with 60 s resolution). Occasional echoes are also seen in the polar cap region, which are from the radar at Rankin Inlet. Representative snapshots from the movie are shown in Figure 2.

As seen in Movie S1 and the first two plots of Figure 2, a narrow band of moderately active aurora lay along the poleward boundary of the evening-to-midnight auroral oval prior to the shock impact. This activity, and the lower than average location of the auroral poleward boundary (magnetic latitude Λ~68°–70°), likely resulted from the prestorm southward IMF of a few nanotesla. The flows seen by the SuperDARN radars show weak, and relatively uniform, east-to-west flow at subauroral midlatitudes (Λ~52° to 62°) as indicated by the

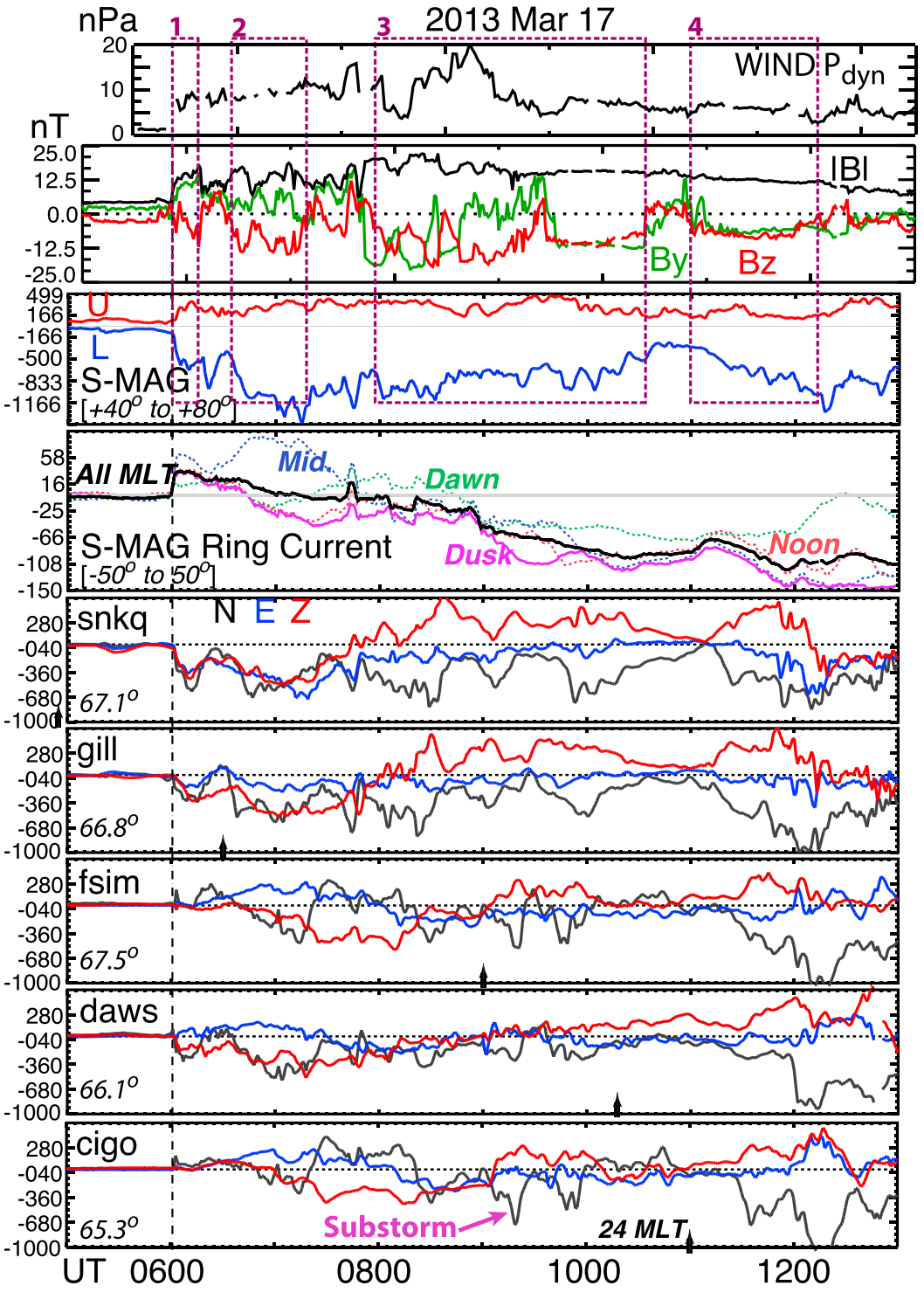

Figure 1. (top to bottom) The Wind P_{dyn}; the OMNI IMF; the SuperMAG upper *U* and lower *L* magnetic indices; the SuperMAG ring current index for all MLT and within the dusk, noon, dawn, and midnight sectors; and ground magnetometer observations from North American stations near 66–67° MLAT with increasing UT of midnight (indicated by small vertical arrows) from CARISMA and the University of Alaska. N and E directions are local magnetic north and east, respectively, and *Z* direction is vertically down. The IMF and P_{dyn} data are shifted so that the shock impact time agrees with the 06:00 UT impact time seen by the ground magnetometers. The maroon dashed boxes identify four main periods of southward IMF seen after the shock arrival.

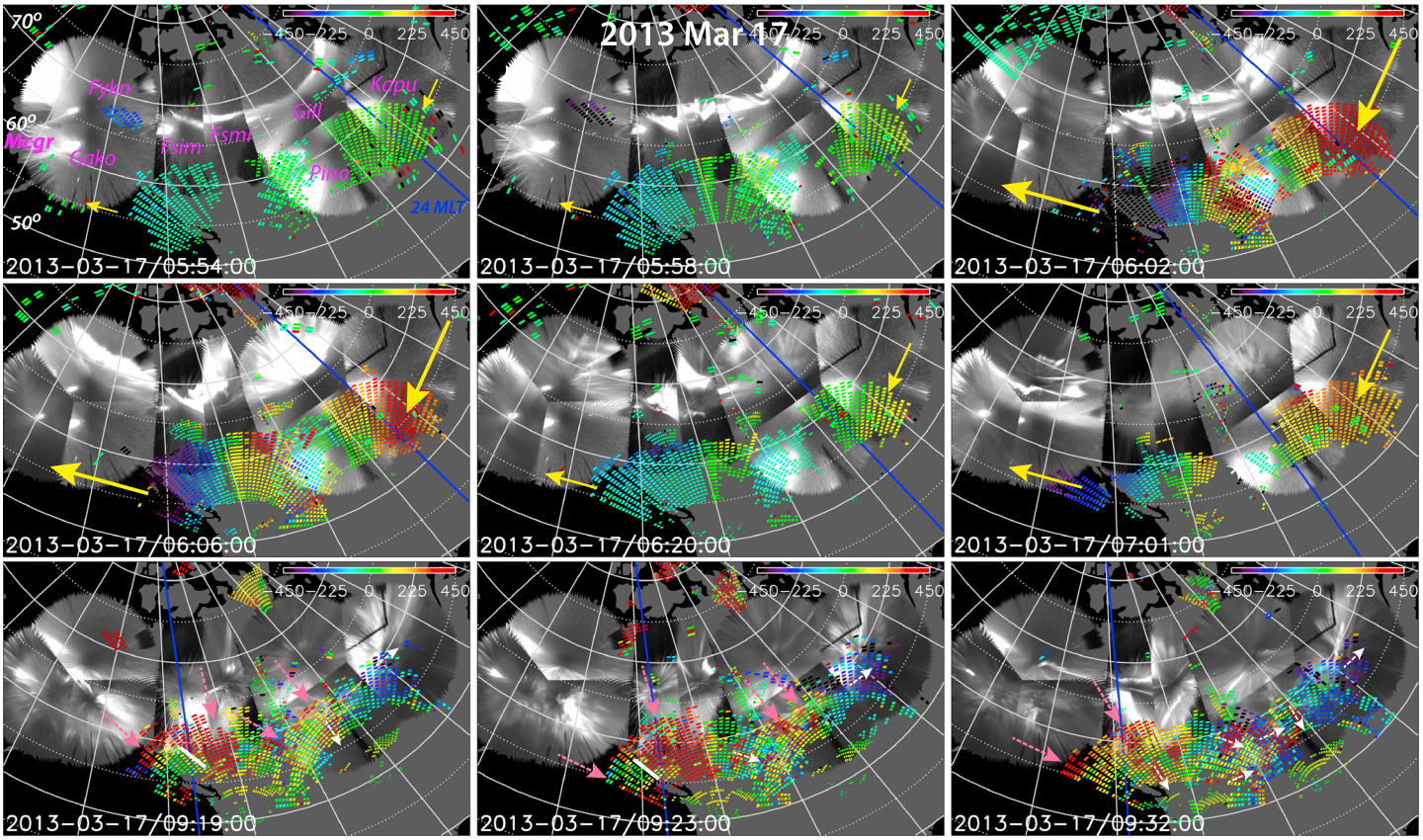

Figure 2. Representative snapshots from Movie S1. Each plot shows the auroral images overlaid with LOS flow velocities from the SuperDARN radars. The images are mergers from all available ASIs over Canada and Alaska, and, from west to east, LOS flow velocities are from the midlatitude CVW, CVE, FHW, and FHE radars. Occasional radar echoes seen in the polar cap region are from the radar at Rankin Inlet. ASI station locations are given in the first plot. The yellow arrows in the top and middle plots illustrate the magnitude of midlatitude westward flow. The pink and white arrows in the bottom plots identify the longitudinally localized flow bursts seen in LOS flows directed toward a radar and eastward flow bursts seen in the easternmost radar echoes. The short white lines in the 09:19 and 09:20 UT plots illustrate the westward excursion of the western edge of a flow burst near midnight.

observed flows being toward the radars in the eastward looking and away from the radars in the westward looking beams.

The dramatic effects of the shock impact can be seen in Movie S1 and the next two plots (06:02 and 06:06 UT) of Figure 2. This includes a rapid, large poleward expansion of the auroral oval over a broad MLT range, which is a well-studied response to dynamic pressure impacts under prior southward IMF conditions [*Boudouridis et al.*, 2003; *Zesta et al.*, 2000]. There is also a very large increase in the midlatitude, subauroral westward electric fields. These penetrating electric fields are part of the well-known global response to solar wind dynamic pressure impacts [e.g., *Hori et al.*, 2012; *Kikuchi et al.*, 2001; *Takahashi et al.*, 2015; *Zesta et al.*, 2000].

The change in the auroral oval precipitation can be seen very clearly in the precipitation observations shown in Figure 3 from DMSP F17 and F16, which, respectively, traversed the southern hemisphere auroral oval and polar cap several minutes before and several minutes after the shock impact. For each spacecraft, integrated precipitating electron energy flux is shown in the top plot and energy-time spectrograms of precipitating electron and ion energy fluxes are shown in the bottom two plots. The auroral arc along the auroral boundary before the shock can clearly be seen as inverted-*V* structures in the F17 data on both the premidnight and postmidnight crossings of the oval, and an ~2.5° wide band of diffuse auroral precipitation can be seen at ~1–10 keV on the postmidnight crossing. This region of diffuse electron precipitation continues to be seen, with a small ~1° equatorward displacement, on the postshock F16 crossing ~18 min later, the energy and fluxes of the precipitating electrons having been increased by the shock compression of the magnetosphere.

However, in addition, the postshock crossing shows a broad region of strong structured electron precipitation, with peak energies within inverted-*V* regions extending to >10 keV. This region extends poleward to

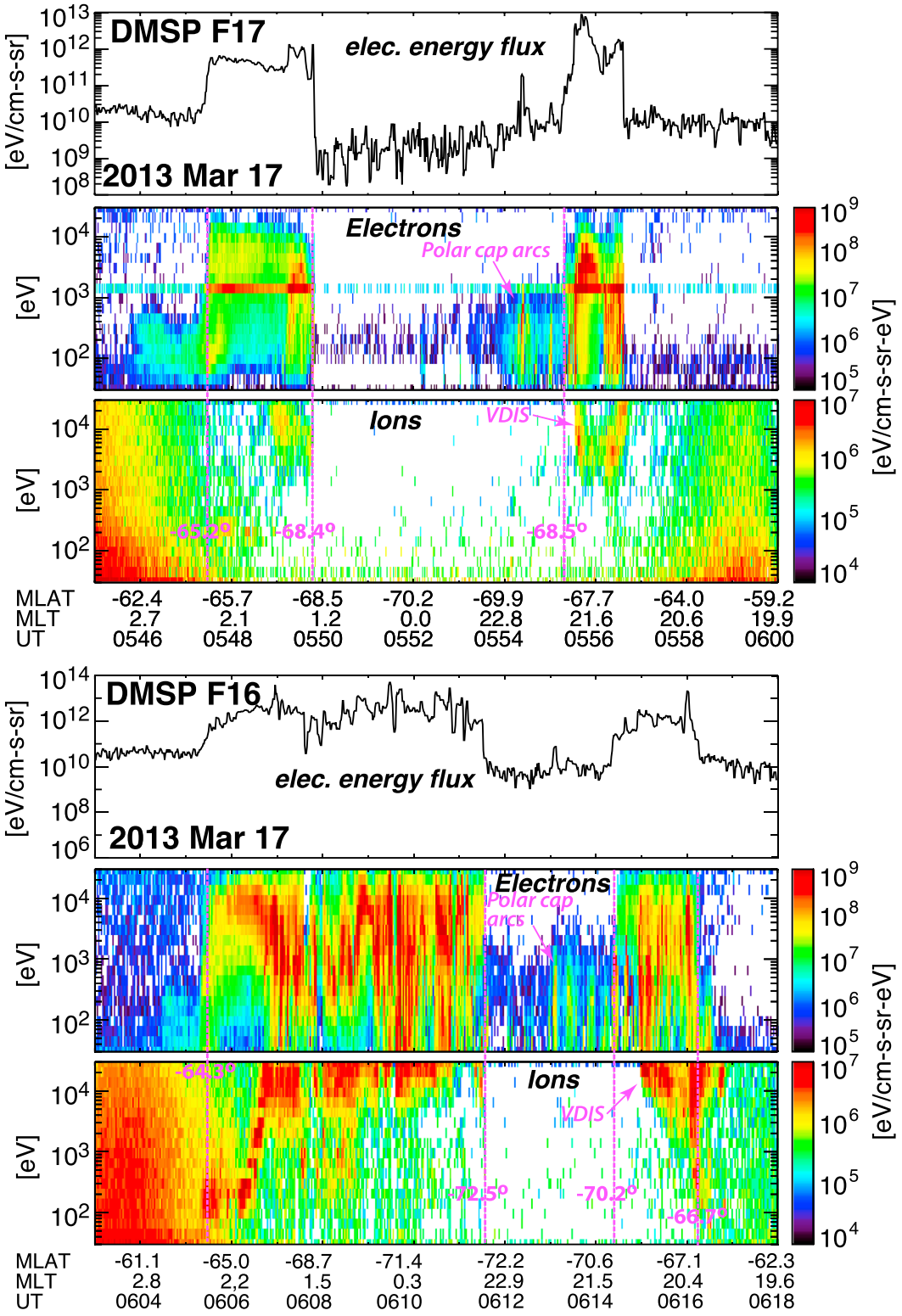

Figure 3. DMSP F17 and F16 observations several minutes before and several minutes after, respectively, the shock impact. For each spacecraft, integrated precipitating electron energy flux is shown in the top plot and energy-time spectrograms of precipitating electron and ion energy flux are shown in the bottom two plots. Latitudes of poleward and equatorward boundaries are given, and a region of weak polar cap arc precipitation is identified.

$\Lambda = 72.5°$ and includes strong precipitation of ~10 to >30 keV protons, indicating that, within the ~10 min period following the shock, a broad, active region of new plasma sheet with high proton energies had formed within an ~4° wide region of previously open lobe field lines. A similar feature is seen on the premidnight crossing but over a substantially narrower ~1.7° wide latitude range. This new particle population, associated with the previously known rapid nightside reconnection across the nightside plasma sheet boundary that is driven by solar wind dynamic pressure impacts [*Boudouridis et al*., 2004, 2005], gives a reservoir of energetic plasma that could be convected earthward in the plasma sheet to become a feature of the storm time disturbance phenomena at lower latitudes.

2.2. Second Southward IMF Period (06:35–07:18 UT)

Figure 4 shows the overviews of the ASI and radar data from 05:00 to 14:30 UT. The top two plots give keograms along a magnetic meridian somewhat to the west/east of the central meridian of the Fort Smith (FSMI)/Pinawa (PINA) ASI (the imager fields of view being shown in Figure 1). The FSMI keogram shows that the rapid poleward expansion and small equatorward expansion of the oval after the shock impact during period 1 were followed by equatorward expansion of the oval to Λ~66° during period 2, the second period of southward IMF. An auroral enhancement at Λ~66° can also be seen to the east in the PINA keogram, where intensities rise to just above background at the end of this time period. The narrow, bright features in the FSMI keogram that extend across several degrees of latitude prior to southward IMF period 2 are keogram signatures of intense auroral streamers. However, such signatures of strong streamers are absent during period 2, and the equatorward expansion appears to be related to that of the diffuse auroral electron precipitation. This different behavior of the aurora between periods 1 and 2 is also apparent in Movie S1.

The bottom four plots of Figure 4 show the LOS velocities of the midlatitude radars that are averaged over two or three beams along the four directions that are drawn in the insert in the top right portion of the figure. The first and third of these plots are from CVW and FHW beams looking northwestward toward the Gulf of Alaska and toward western Canada, respectively. The second is from CVW beams looking approximately poleward toward FSMI, and the fourth plot is from FHE beams looking northeastward over eastern Canada. The large blue dots give the equatorward boundary of plasma sheet electron precipitation as observed on the multiple crossings of the southern hemisphere auroral by the DMSP F16–F18 spacecraft, the MLT of observation given in blue above each dot. Premidnight crossings are shown in the poleward looking CVW plot, although these radar beams are only at premidnight MLTs until ~09:00 UT, and postmidnight crossings are shown in the plot for the eastward looking FHE beams, which measure postmidnight after ~06:00 UT. The modest equatorward expansion of the auroral oval is seen following period 2 in the electron precipitation boundaries between periods 2 and 3. That the precipitation boundaries are a few degrees equatorward of the detectable auroral boundary on the premidnight side is likely a result of the ASI detection threshold. As expected from particle drifts, the electron precipitation boundary is seen a few degrees further equatorward on the postmidnight side, where the DMSP crossings are dawnward of the PINA field of view at times prior to period 3.

As seen by the CVW and FHE radar beams in Figure 4 and the 06:20 and 07:01 UT plots of Figure 2, after decreasing substantially during the northward IMF in between periods 1 and 2, there was a very large increase in the midlatitude, subauroral westward flows during period 2. While the flow speeds were similar to those seen during period 1, there was a distinct difference in the structuring of the convection. During the first period, the LOS plots in Figure 4 looked striped as a result of substantial flow variations that can be seen within the 60 s period from one radar scan to the next. These strong variations can be seen over many more radar beams in Movie S1. On the other hand, the flow had far less structuring during period 2. It is interesting that a similar difference between the two periods is seen in the auroral observations at much higher latitudes, there being several short-lived bright features on the FSMI keogram during period 1 but only much more smoothly varying aurora during period 2. Consistent with the rapidly varying auroral activity seen during period 1, the DMSP F16 electron precipitation observations in Figure 3 show a large number of close-together, strong electron precipitation features.

2.3. Third Southward IMF Period (07:57–10:34 UT)

During the first 1.25 h of southward IMF period 3, the equatorward boundary of the aurora moved several degrees equatorward, from Λ ~66° to Λ ~60° in the PINA keogram. Furthermore, much more streamer

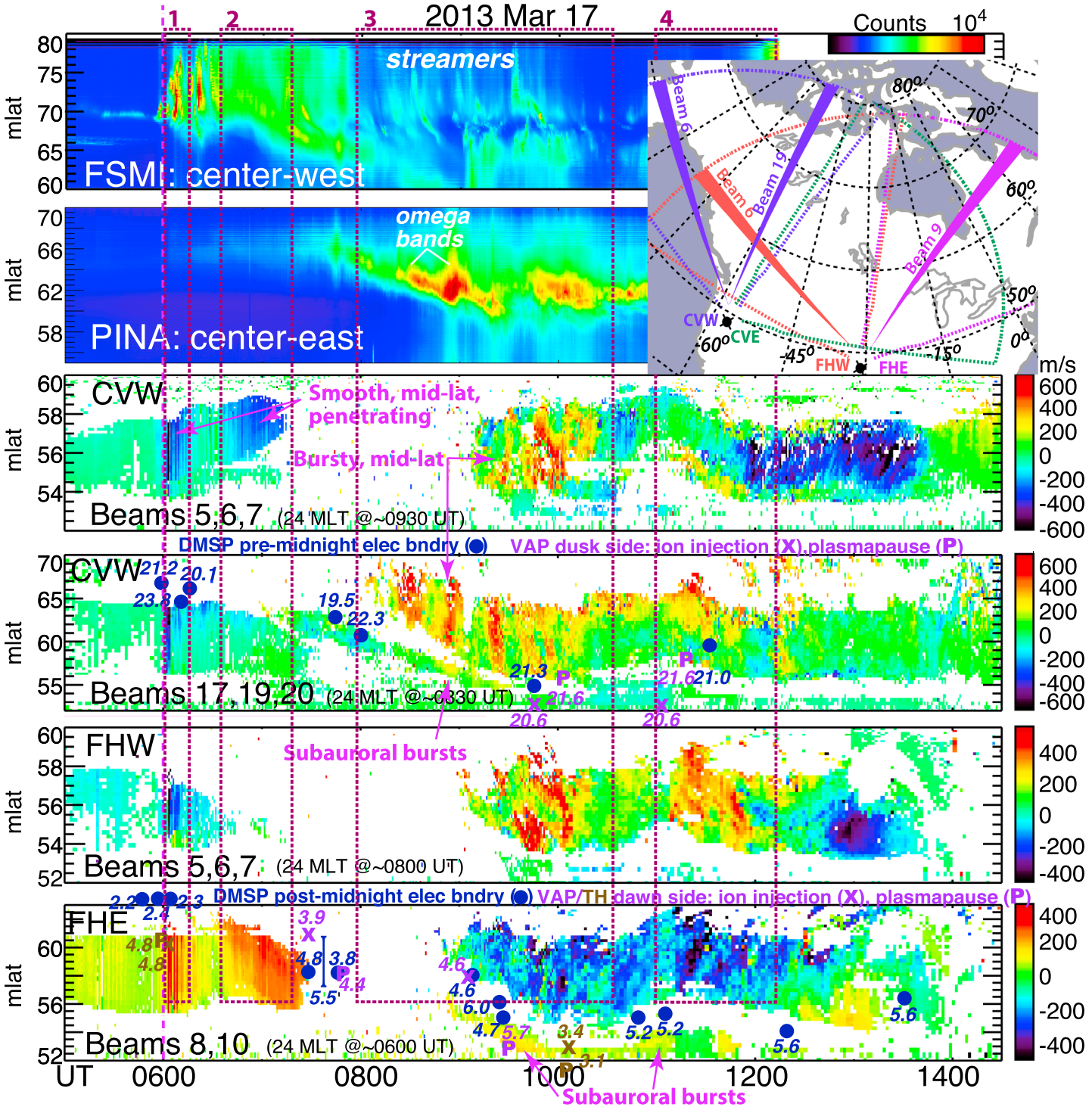

Figure 4. Overviews of the ASI and radar data from 05:00 to 14:30 UT. The top two plots give the keograms along a magnetic meridian somewhat to the west (east) of the central meridian of the FSMI (PINA) ASI. The imager fields of view are shown in Figure 2. The bottom four plots of Figure 4 show the LOS velocities of the midlatitude radars that are averaged over two to three beams along the four directions shown in the insert in the top right corner. The heavy blue dots give the equatorward boundary of plasma sheet electron precipitation observed on southern hemisphere crossings by DMSP F16–F18 spacecraft, the MLT of observation given in blue above each dot. Mapped Λs for the inner edge of ion injection and the plasmapause location are shown with magenta and brown *X*s for the ion edges and *P*s for the plasmapause from the VAP and THEMIS spacecraft, respectively, in the equatorial plane. The maroon dashed boxes identify the four main periods of southward IMF seen after the shock arrival. "Bndry" is the abbreviation for "boundary."

activity occurred during period 3 than during period 2, as can be seen in Movie S1 and the FSMI keogram. Also, a couple of omega bands become apparent at $\Lambda <$ ~64° in the auroral observations from PINA, omega bands being a common feature on the morningside during periods of enhanced convection. The streamers continued throughout period 3, although they were not as intense and close together as during the postshock period 1. Due to light contamination at lower latitudes, the streamers are seen only to Λ ~67° by the FSMI keogram, but a few streamers can be discerned in S1 that extended to Λ ~62°.

Very different midlatitude convection features were seen during period 3 as compared to what was seen during period 2. As can be seen for all the beams in Figure 4, the convection became very bursty with LOS flow speeds varying from ~500 m/s to close to 0 m/s repetitively over ~10–20 min periods. These bursts of enhanced flow have a strong equatorward component as shown by the poleward looking CVW beams (17,19,20), and the strong bursty behavior of the flows continues into the region of postmidnight eastward flows seen in the FHW and FHE plots. While these radar echoes are at the same midlatitudes as during periods 1 and 2, the regions of echoes appear to move equatorward with the equatorward boundary of the aurora, particularly in the poleward looking CVW plot. This suggests that these midlatitude echoes are within the expanding aurora oval, consistent with the equatorward boundaries of electron precipitation seen by the DMSP spacecraft.

As indicated by the pink and white arrows in the bottom plots of Figure 2, each individual flow burst during period 3 had a longitudinal width $\lesssim$1 h in MLT, some being «1 h in MLT. Additionally, based on the LOS flow speeds, many individual bursts did not extend across the full latitudinal extent of the radar echo region. While we are unable to track the two-dimensional evolution of individual flow bursts as function of time with only the LOS flows and 1 min time resolution, the existence of eastward going bursts on the dawnside of the echo region suggests that many flow bursts on the morningside turn azimuthally toward the east. We do not have sufficient echoes during period 3 to determine if evening side bursts turn toward the west as has previously been seen [*Kauristie et al*., 2003; *Zou et al*., 2009]. However, there is evidence for a westward excursion of flow bursts near midnight, as indicated by the short white lines in the 09:19 and 09:20 UT plots of Figure 2.

Additionally, there are some radar echoes during period 3 that appear to be subauroral and show bursty flows, as identified in Figure 4. These have an equatorward component as seen by the poleward looking CVW beams and a westward component in the eastward looking FHE beams. These flows are almost certainly within the subauroral polarization stream (SAPS) region, since the flows lay equatorward of the equatorward DSMP electron precipitation boundaries. The fact that these flows are bursty is consistent with some of the flow bursts within the auroral oval extending equatorward into the SAPS region and turning toward the west. We thus see evidence for a general guiding of the flow bursts by the large-scale convection pattern, flow bursts within the duskside convection being azimuthally turned to the west (some within the SAPS region), and those within the dawn cell being turned toward the east, consistent with recent implications from observations [*Lyons et al*., 2015].

2.4. Fourth Southward IMF Period (11:00–12:13 UT)

The bursty flow pattern continued during southward IMF period 4, the pattern being very similar to that during period 4. Enhanced bursts of flow can be seen in the equatorward and eastward flows, as well as in the westward subauroral flows. However, based on the DMSP equatorward electron boundaries in Figure 4 and the Alaskan ASI images in Movie S1, the equatorward boundary of the auroral precipitation did not expand discernibly further equatorward during this period.

3. Equivalent Ionospheric and Field-Aligned Current Systems

The radar observations have indicated the existence of three different modes of midlatitude electric field enhancements following the storm shock and during the storm main phase. In this section, we show how the postshock, smoothly enhanced, and bursty enhanced convection modes are reflected in ionospheric and field-aligned current systems. Figure 5 shows the ionospheric equivalent currents over North America obtained from ground-based magnetometers (locations given by yellow stars) using the spherical elementary current system (SECS) approach [*Amm and Viljanen*, 1997; *Weygand et al*., 2011]. The top plot reproduces the poleward looking CVW plot from Figure 4, the four southward IMF periods being identified by maroon dashed lines and vertical magenta lines identifying the times of the SECS plots in the bottom two rows.

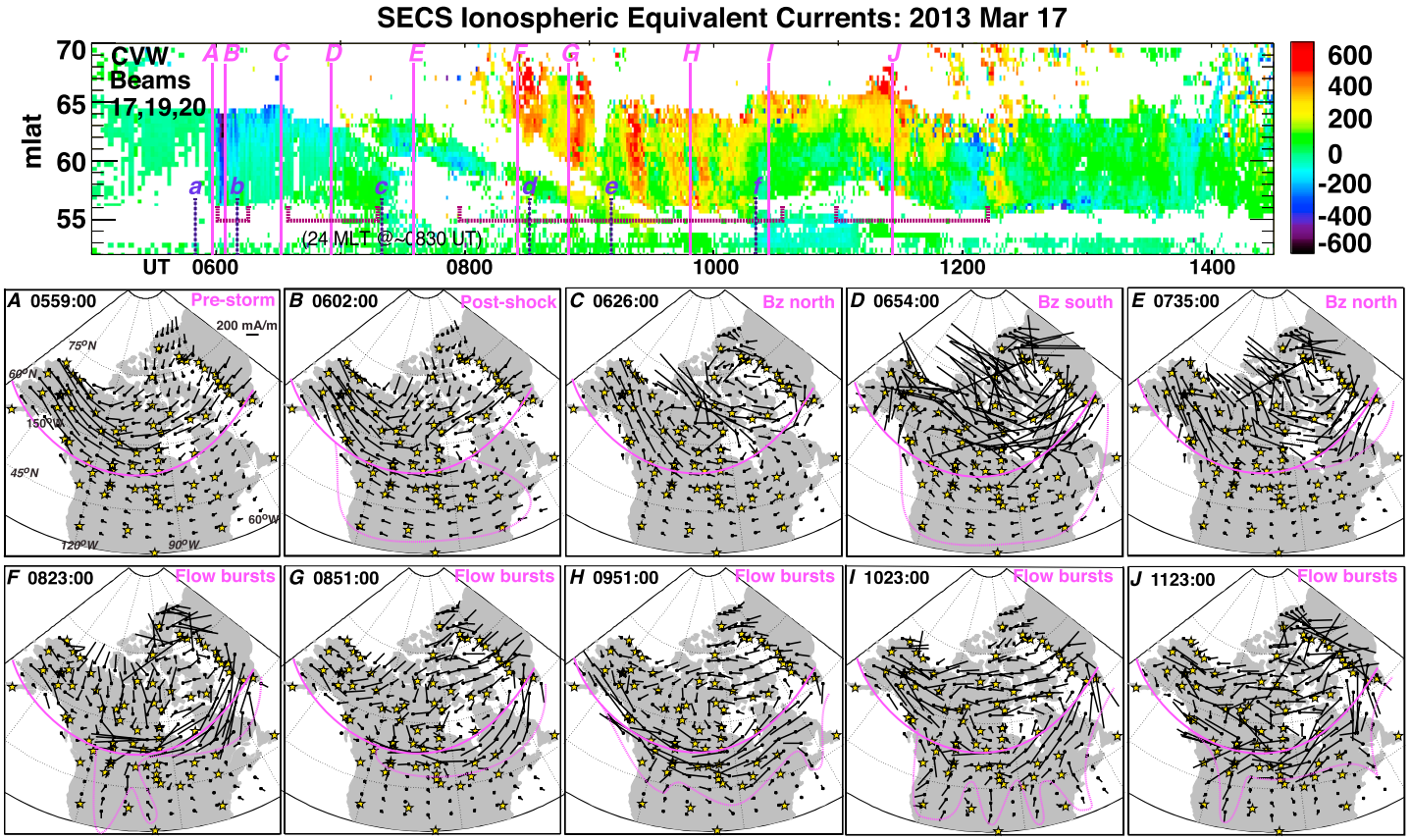

Figure 5. Ionospheric equivalent currents over North America obtained from ground-based magnetometers (locations given by yellow starts) calculated from SECS method. The top plot reproduces the poleward looking CVW plot from Figure 2, the maroon dashed lines identify the four southward IMF periods, the vertical magenta lines identify the times of the SECS plots in the bottom two rows, and the blue dashed vertical lines identify the times of the AMPERE plots in Figure 6. The preshock eastward current of the duskside DP2 cell in plot A lies at Λs above the magenta solid curve, which is repeated in subsequent plots for reference. In subsequent plots, a dashed magenta line outlines the region of enhanced currents at Λs below the solid magenta line.

The first equivalent current plot shows the preshock eastward current of the duskside DP2 cell lying at $\Lambda \gtrsim 68°$ (above the magenta solid curve, which is repeated in subsequent plots for reference). Just after the shock, as seen in the SECS plot B, eastward currents became enhanced at almost all longitudes at Λs below the solid magenta line to the lowest Λ of observation (~42°). A dashed magenta line outlines this region. This plot shows the ionospheric currents of the enhanced penetrating electric fields seen by the radars, as expected, and also shows that they extended to much lower latitudes than could be seen by the radars. The midlatitude currents returned to near their preshock configuration level during the northward IMF interval between periods 1 and 2 (plot C). They then increased again during southward IMF period 2 (plots D and E), indicating that the penetrating electric field pattern during period 2 was similar to that during period 1. At higher latitudes, the dawnside DP2 current cell, as well as the duskside cell, became visible over North America, as did the sunward current between the duskside and dawnside cells.

During the periods 3 and 4 of longitudinally narrow, bursty flows (plots F–I), the ionospheric equivalent currents became substantially different than during the previous intervals. In particular, longitudinal narrow regions of current appear to extend to the lowest Λ of observation. It should be noted, however, that there are an insufficient number of magnetometer stations to accurately discern the longitudinally dependent details of the current structure, particularly at $\Lambda s < 45°$, where longitudinal coverage is limited. However, it is clear that the currents have more longitudinal structure than during the earlier periods, indicating that the associated longitudinally structured electric fields penetrated to Λs at least 10° equatorward of the equatorward boundary of auroral electron precipitation as seen by the DMSP spacecraft observations in Figure 2. Such electric fields have the potential for injecting particles to low *L* shells during this storm main phase.

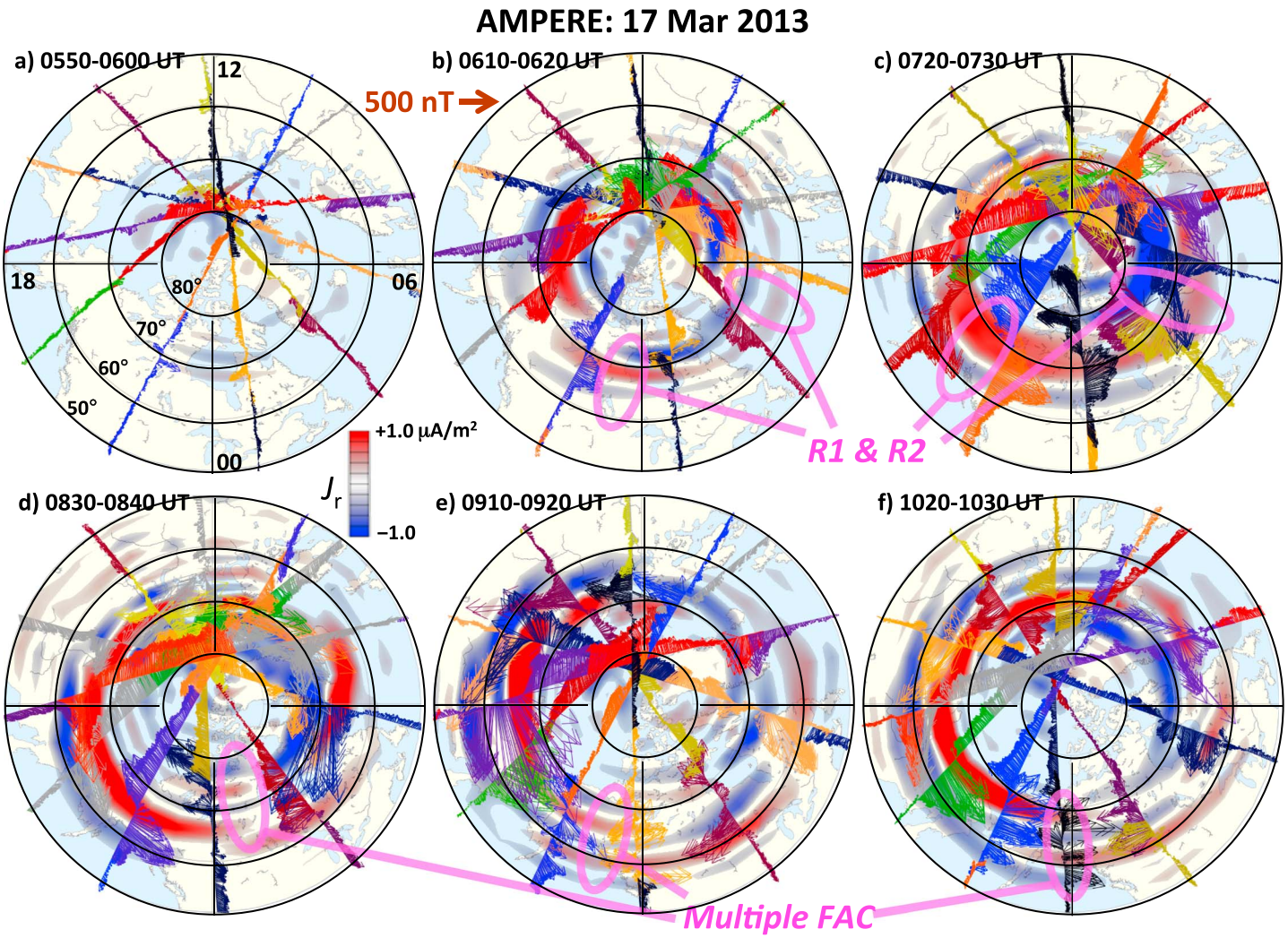

Figure 6. (a–f) Magnetic perturbations observed along Iridium satellite trajectories during the 10 min intervals identified by blue dashed vertical lines in the top plot of Figure 5. The red and blue shadings give the upward and downward radial currents, respectively, obtained from the curl of fits to the magnetic perturbations.

Figure 6 shows the AMPERE magnetic perturbations observed along Iridium satellite trajectories during the 10 min intervals identified by blue dashed vertical lines (Figures 6a–6f) in the top plot of Figure 5. Red and blue shadings give upward and downward FACs, respectively, obtained from the curl of fits to the magnetic perturbations [*Waters et al.*, 2001]. The currents are denoted as J_r, since they are actually radial, being calculated from the curl on a spherical surface. It can be seen that field-aligned currents were weak just before the shock impact (Figure 6a). A well-defined region 1 (R1) and R2 FAC pair formed during the postshock period 1 (Figure 6b), the duskside R2 currents extending equatorward to Λ~62°, which is ~3° equatorward of the equatorward boundary of electron precipitation during the period as seen by the DMSP boundaries in Figure 4, consistent with these being the downward currents that are driven by the partial ring current and give rise to SAPS. During the period of smoothly enhanced convection (period 2; Figure 6c), the well-defined R1 and R2 current system amplified, and extended equatorward by ~1–2°, which is similar to the equatorward expansion seen in the duskside DMSP spacecraft equatorward boundaries after period 2 but before period 3.

As with the ionospheric equivalent currents, the FACs became significantly different during period 3 (Figures 6d–6f) than at earlier times. While the current fitting procedure significantly smooths longitudinal variations, the current system near midnight changes from that of the typical R1-R2 system to one of multiple, smaller-scale currents, consistent with the increased structuring seen in the electric fields and the ionospheric equivalent currents. The latitudinal structuring is most evident in the magnetic perturbation vectors, which

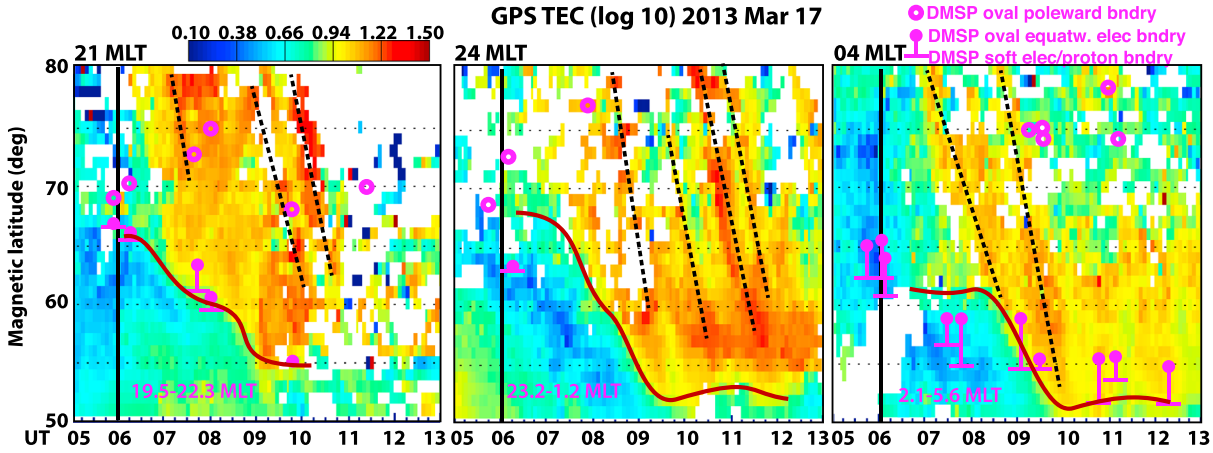

Figure 7. TEC measurements at 21:00, 24:00, and 04:00 MLT from available ground GPS stations as a function of Λ and UT. The magenta dots identify the equatorward boundary of plasma sheet electron precipitation, based on precipitating electron energy flux of 10^{10} eV/(cm^2 sr s), and the magenta circles give the poleward of auroral particle precipitation. The magenta bars extending to lower latitudes give the equatorward boundary of less intense, but detected, plasma sheet proton (<23:00 MLT) or soft electron (>23:00 MLT) precipitation, which extended to somewhat lower latitudes than did the main plasma sheet electron precipitation. The dashed diagonal lines identify the clearest equatorward moving TEC enhancement features. "Bndry" is the abbreviation for "boundary."

exhibit multiple east-west reversals along one or more tracks near midnight. Significant magnetic perturbations extend to Λ~52° in Figures 6e and 6f, which is where the subauroral bursts are seen in the radar data in Figure 4.

4. Ionospheric Densities Revealed by Vertical TEC and PFISR

TEC measurements at 21:00, 24:00, and 04:00 MLT from available ground GPS stations are shown in Figure 7 as a function of Λ and UT. Magenta dots identify the equatorward boundary of plasma sheet electron precipitation, based on precipitating electron energy flux of 10^{10} eV/(cm^2 sr s), and magenta circles give the poleward boundary of auroral particle precipitation (i.e., of electron precipitation, since its poleward boundary was at or poleward of the proton boundary). Magenta bars extending to lower latitudes give the equatorward boundary of less intense, but detected, plasma sheet proton (<23:00 MLT) or soft electron (>23:00 MLT) precipitation, which extended to somewhat lower latitudes than did the main plasma sheet electron precipitation.

TEC values were low prior to the shock impact, and there may have been a small increase at $\Lambda \gtrsim 67°$ after the shock. The largest TEC values are seen after ~07:00 UT and appear as features that move equatorward from the highest latitude shown ($\Lambda = 80°$). This latitude appears to be within the polar cap, several degrees poleward of the poleward boundary of the auroral oval as indicated by the DMSP measurements, the auroral observations in Movie S1, and the poleward boundary of R1 field-aligned currents in Figure 6. However, we note that the poleward boundary of the oval is not very clear in the auroral images and that there are uncertainties in using the southern hemisphere DMSP values for the poleward boundary in the northern hemisphere. Thus, there are some uncertainties in our determination of the auroral poleward boundary. The equatorward boundary of the TEC enhancements, which also represents the poleward boundary of the midlatitude trough, moves equatorward after ~07:00 UT, in approximate agreement with what is seen for the auroral oval electron precipitation by DMSP and the auroral imagers, as has previously been reported by *Zou et al.* [2011]. Additionally, the equatorward boundary of the midlatitude trough appears to move equatorward in the 24:00 MLT plot, although examination of the TEC at all MLT indicates that this may be related to azimuthal motion of a longitudinal feature.

The equatorward moving TEC enhancement features, having the characteristics of polar cap patches, are seen within the auroral oval (based on being equatorward of the DMSP poleward boundaries) from ~07:30 to ~12:00 UT. Electron density and temperature profiles measured by PFISR (Figure 8) in the premidnight sector (10:00–11:15 UT) confirm the typical patch signatures (enhanced densities above 300 km and lower electron temperature than of the surrounding auroral features) as structures moving equatorward

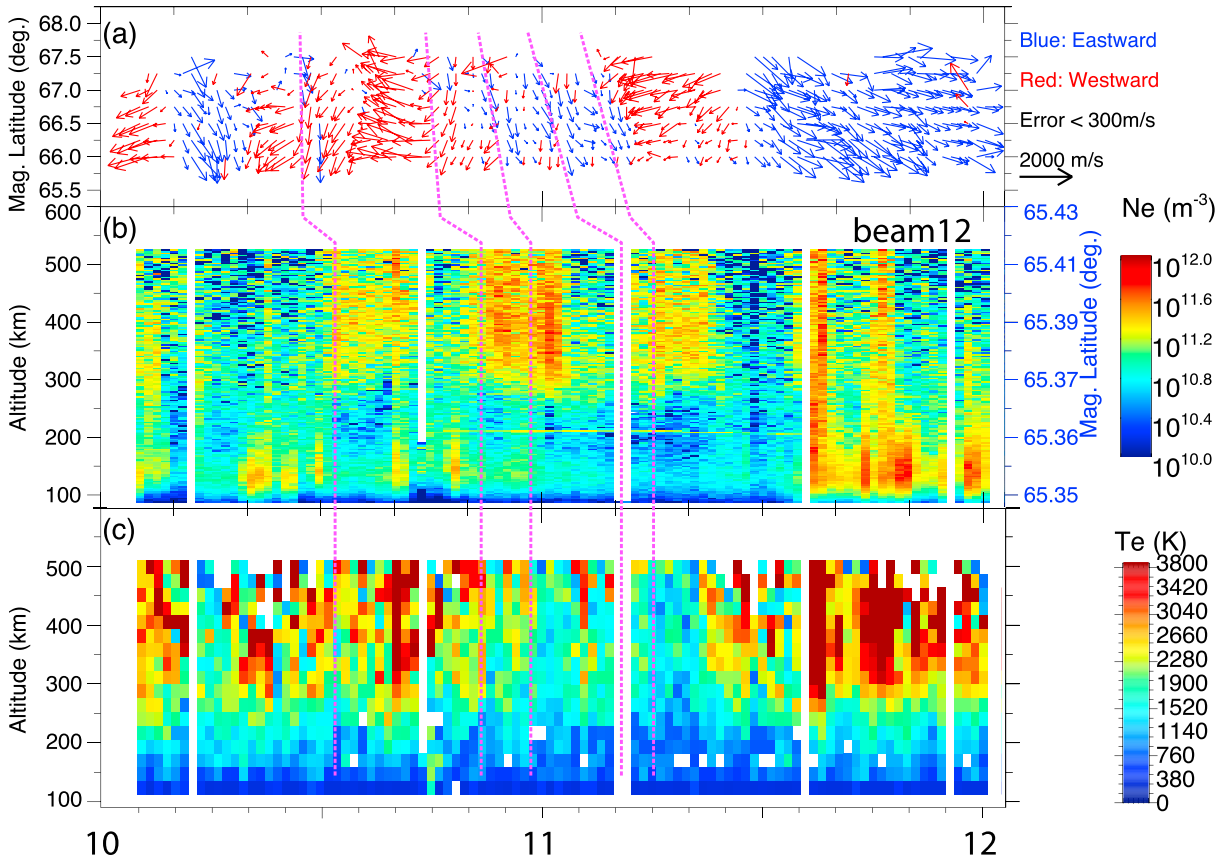

Figure 8. PFISR measurements on 17 March 2013 as a function of magnetic latitude and universal time. (a) Nightside convection flow vectors with a measurement uncertainty <300 m/s. (b) Raw electron densities with no correction for T_e/T_i or Debye length effects measured by beam 12 (upward along the magnetic field). Altitude is indicated on the left *y* axis, and magnetic latitude is indicated on the right *y* axis. (c) Electron temperature measured by the beam 12 long-pulse mode. The dashed magenta lines indicate the start of patches as marked by enhanced *F* region densities above ~300 km with reduced T_e, and the patch connection equatorially directed flow bursts.

across the PFISR field of view. The clearest of these are identified by dashed diagonal lines. This roughly corresponds to southward IMF periods 3 and 4, during which convection was dominated by flow bursts. These density enhancement features appear to move from the polar cap to the auroral oval as has previously seen by *Zhang et al.* [2013] and from simulation results by *Crowley* [1996]. That they occur during the period of flow bursts suggests that the enhancements are brought into the auroral oval by flow channels from the polar cap that cross the open-closed field line boundary and enter the plasma sheet. Such entry of polar cap flow bursts into the plasma sheet is now believed to be a common feature that leads to plasma sheet flow bursts, giving rise to auroral poleward boundary intensifications and streamers [*de la Beaujardière et al.*, 1994; *Lyons et al.*, 2011; *Nishimura et al.*, 2010; *Pitkänen et al.*, 2013; *Shi et al.*, 2012; *Zou et al.*, 2014], and would be expected to carry the TEC enhancements equatorward within the auroral oval.

Consistent with the TEC flux enhancements being transported equatorward by flow bursts, the radar flow vectors in Figure 8 show that equatorward flow bursts were seen by PFISR at $\Lambda = 66$–$67.5°$ a few minutes before the patches appeared in the densities along the local magnetic field line ($\Lambda = 65.4°$, beam 12). To explore the possibility further, Figure 9 shows the TEC and LOS flows along four radar beams. The beams were selected to maximize overlapping coverage of TEC measurements and radar echoes as well as to illustrate various features of interest, and each TEC measurement has been averaged over the three adjacent beams centered on the beam illustrated in the top left hand corner. For each beam, thick horizontal dashed lines identify a Λ in both the LOS and TEC plots that has been selected to maximize overlapping flow burst and TEC enhancement coverage. Thinner dashed vertical lines give visually estimated times of the initiation of flow burst crossings of the horizontal lines.

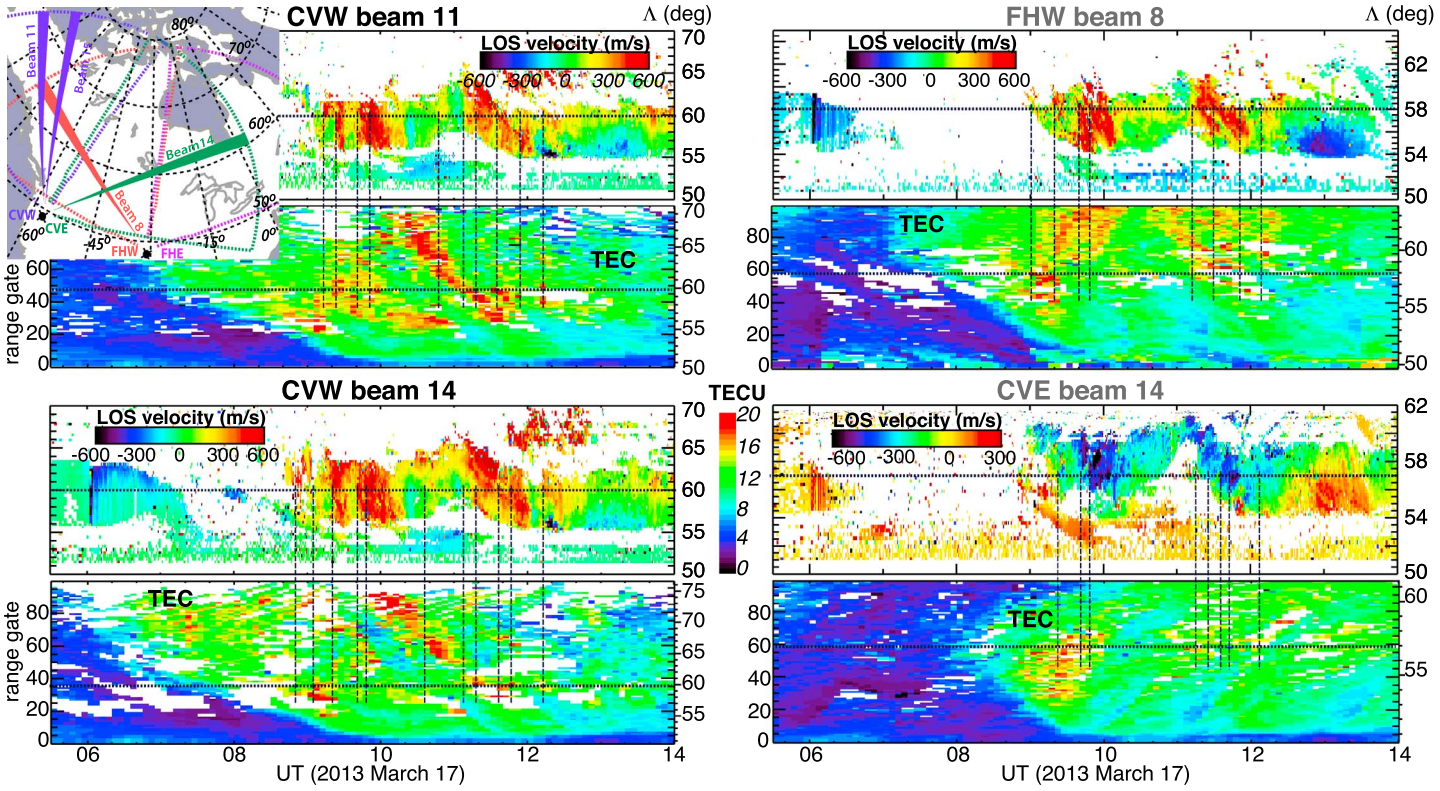

Figure 9. TEC and LOS flows averaged over the three adjacent beams centered on the beam illustrated in the top left hand corner. For each beam, the thick horizontal dashed lines identify a Λ's in both the LOS and TEC plots selected to maximize overlapping flow burst and TEC enhancement coverage. The thinner dashed vertical lines give visually estimated times of the initiation of flow burst crossings of the horizontal lines.

As seen in the auroral oval, flow bursts extend over several degrees of latitude as they move both equatorward and azimuthally through the plasma sheet. Thus, apparent motion of TEC and flow burst features along a radar beam reflects how both their equatorward and azimuthal flow leads to crossing of that beam. If the TEC enhancements are carried by the flow bursts, there should be an association between their crossing of the radar beam and that of the flow bursts. Such an association seems clear from the CVW west beams on the left side of Figure 8, which look north-northwestward. These beams give the best views of density structures having a beam crossing that moves equatorward with time, beam 11 having better TEC coverage and beam 14 having broader LOS velocity coverage. While there is not a precise one-to-one association between the flows and the TEC enhancements, there is a general association between the time intervals of flow bursts and of TEC enhancements (~08:45–12:15 UT). Furthermore, a TEC enhancement is seen near most of the locations where the vertical dashed lines (at $\Lambda = 60°$) crosses the horizontal dashed line, and most of TEC enhancements along the dotted line occur near these crossings.

FHW beam 8 looks northwestward and saw flow bursts having a beam crossing location that moved equatorward with time. The horizontal line shown in this plot is at $\Lambda = 58°$ and at a beam location a little more than 1 h to the east of that for the line shown in the CVW plots. Similar features are seen as for the CVW beams, though with a more clear association between the two time periods of LOS flow and TEC enhancements, from ~09:00 to 10:00 and from ~11:00 to 12:00 UT, and the clear gap in between. The CVE beam looks east-northeastward and thus sees the flow bursts as away from the radar flows (blue color) moving eastward in the dawn convection cell. The crossing of the radar beam by these flow bursts moves to higher latitudes (further range gates) with time, which reflects the bursts eastward motion within the dawn convection cell. The TEC enhancements also show such motion of their crossings of the radar beam to higher-range gates. Furthermore, as with the FHW beam, there is clear association between the two regions on LOS flow and TEC enhancements and a clear gap in between. Both of these features along the CVE beam support the suggestion that the TEC enhancements are carried with the auroral oval by the flow bursts.

Figures 7–9 give evidence that the flow bursts bring TEC enhancements from the polar cap into the plasma sheet. These enhancements are brought further and further equatorward during periods 3 and 4 to near the equatorward boundary of the auroral, and this occurs at the same as the flow bursts also expand the auroral oval equatorward to Λ's below 55°. We note that the evidence from Figures 7–9 is qualitative, so that it would be desirable develop a more quantitative comparison between the flow bursts and TEC enhancements. This would require taking into account the LOS nature of the SuperDARN flow velocities and the tendency for high TECs to be associated with enhanced radar backscatter, a tendency that can be seen in Figure 8.

5. Ring Current Particle Injection

The equatorward expansion of the auroral oval should correspond to an earthward motion of the inner edge of the plasma sheet. The plasma sheet particles, energized with the increasing magnetic field strength as the flow bursts move them earthward, should be expected to become part of the storm time ring current. We examine this possibility by examining the equatorial Van Allen Probes (VAP) particle observations. VAP-B preceded VAP-A as they both moved inbound in the postmidnight sector and outbound in the premidnight sector.

Figure 10 shows the time profiles of electrons and ions measured by the Magnetic Electron Ion Spectrometer (MagEIS) instrument [*Blake et al*., 2013] from the last VAP pass (VAP-B outbound) before the storm shock impact (top), the next VAP-B and VAP-A passes (inbound and outbound) during the storm main phase (middle), and the subsequent inbound and outbound passes during the beginning of the storm recovery phase (bottom). The quiet time passes show the typical quiet time structure of the ring current ions, their outer zone peak moving earthward with increasing energy, and of the ring current and radiation belt electrons with their two-zone structure. The flux enhancement due to the 06:00 UT shock impact was seen at $L \simeq 6$ on the VAP-B inbound pass.

On each postshock pass, the inner edge of ion injection as seen in the line plots is identified with a solid maroon line, and the location of the plasmapause based on the density measurements (inferred from the upper hybrid resonance line using the Electric and Magnetic Field Instrument Suite and Integrated Science (EMFISIS) wave measurements [*Kletzing et al*., 2013; *Kurth et al*., 2015]) is identified by a dotted dark green line. The electron data show the approximate correspondence between their inner injection boundary and that of the ions. On the first VAP-B inbound pass, the ion injection edge and the plasmapause can be seen at ~07:30–08:00, just after period 2. They were located at $L = 4.2$ and 3.5, respectively, which is somewhat earthward from their typical quiet time location. The subsequent VAP-A pass observed the boundaries at ~09:00–09:30 UT and shows that they had moved ~0.7 R_E further earthward during the first half of period 3. As seen in the profile for the outbound portions of these passes, and additional ~0.9 R_E of inward motion was seen for the ion inner edge during the remainder of period 3. However, some of this later inward motion was likely an MLT effect from particle drift trajectories, as can be seen by the ion edge being earthward of the plasmapause on the duskside. The recovery phase orbit shows that a further few tenths of an R_E earthward penetration occurred during, or somewhat after, the flow burst period 4. Similar locations for the inner edge of ion injection can be seen in Figure 3 of *Gkioulidou et al.* [2014], where it is also seen that the peak in ring current pressure moved into L~3.5, consistent with what is expected for a storm of the strength [e.g., *Antonova*, 2006; *Antonova and Stepanova*, 2015].

Each observed L value was mapped to a dipole field (which is valid at these low Ls). The corresponding Λs are shown by magenta Xs for the ion edges and Ps for the plasmapause in Figure 4, with the addition of the corresponding Λs from the equatorial THEMIS spacecraft given by brown Xs and Ps. Values from duskside (dawnside) portions of spacecraft orbits are shown in the more duskside CVW plot (beams 17,19,20) and the more dawnside FHE plot, respectively. The MLT of each observation point is also indicated.

Very near the time of the shock impact, the THEMIS spacecraft showed the boundaries laying a few degrees equatorward of the DMSP electron precipitation boundaries, likely representing previous weak activity. Based on the dawnside THEMIS and VAP passes, little equatorward motion was seen during periods 1 and 2, with most of the equatorward motion of the boundaries occurring during period 3. This is consistent with what is seen in the DMSP boundaries, the radar echo boundaries, and the auroral observations. These observations indicate that the large majority of the injections of ring current particles to lower L occurred during the flow-burst time period of most rapid and furthest equatorward penetration of the auroral oval and associated

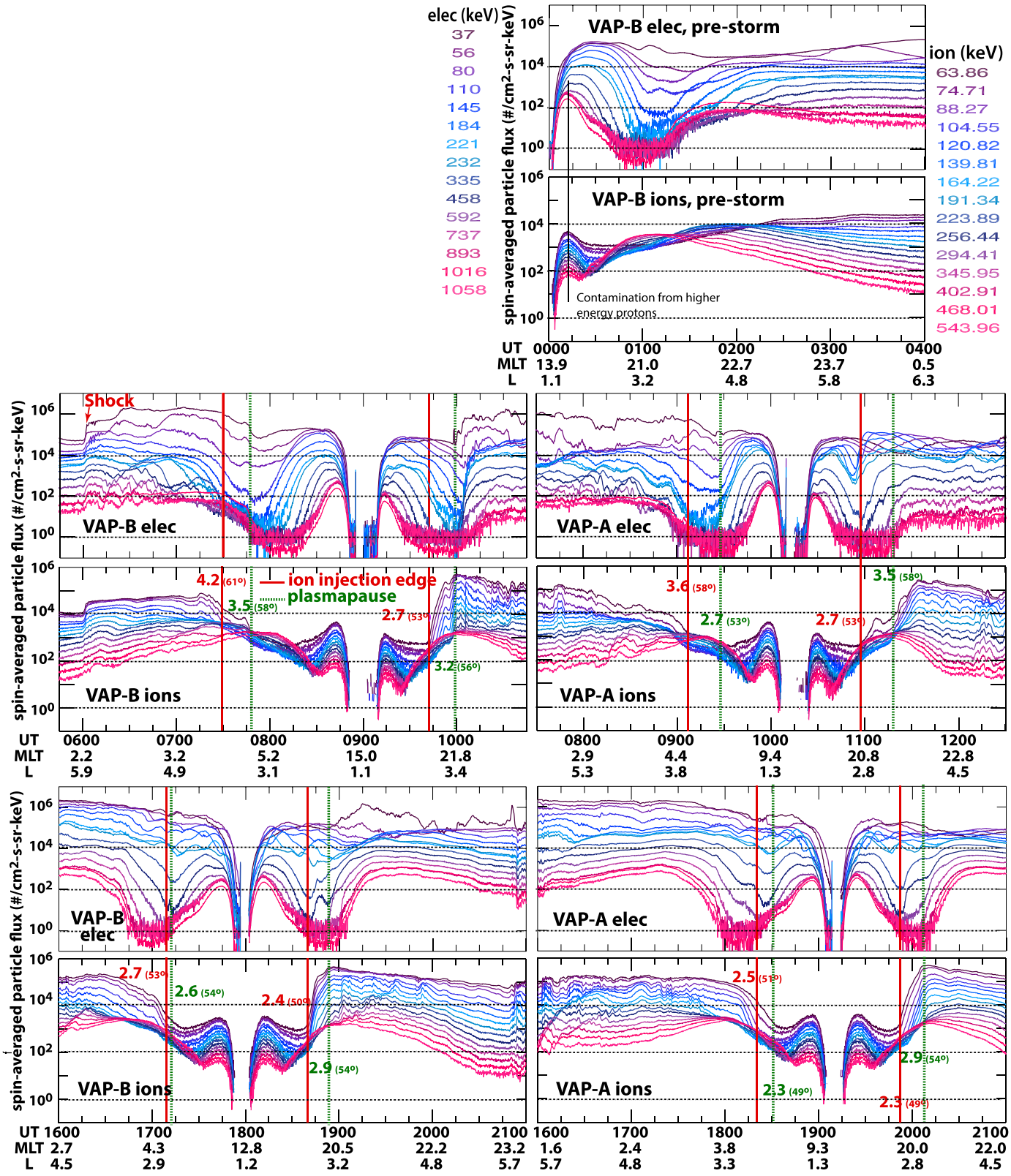

Figure 10. Time profiles of electrons and ions from (top) the last VAP pass (VAP-B outbound) before the storm shock impact, (middle) the next VAP-B and VAP-A passes (inbound and outbound) during the storm main phase, and (bottom) the subsequent inbound and outbound passes during the beginning of the storm recovery phase. On each postshock pass, the inner edge of ion injection as seen in the line plots is identified with a solid maroon line, and the location of the plasmapause based on the density measurements is identified by a dotted dark green line. *L* values and mapped Λs for each of these boundaries are identified.

currents. This inference is consistent with observations [*Gkioulidou et al*., 2014] and modeling [*Yu et al*., 2014] of this storm that indicate the importance of multiple ion injections to the formation of the ring current during the storm main phase.

6. Summary

Taking advantage of the excellent coverage of the 17 March 2013 storm main phase from ground-based instruments and from low- and high-altitude spacecraft, we have evaluated the driving of fundamental main-phase phenomena and found evidence for common driving of the auroral oval, nightside ionospheric currents, the R2 field-aligned current system, ionospheric densities, and injection of particles to form the storm time ring current. The storm shock impact drove activity almost immediately: dramatic poleward expansion of the poleward boundary of the auroral oval, strong auroral activity, and strong penetrating midlatitude convection and ionospheric currents. Equatorward expansion of the auroral oval was limited. The dramatic poleward expansion, which implies rapid reconnection along the nightside polar cap boundary, is associated with a broad, active region of new plasma sheet with high proton energies that appears to have formed within a region of previously open lobe field lines. Additionally, a very large increase in the midlatitude, subauroral westward electric fields was observed.

After the initial ~15 min period 1 of southward IMF, there was a less active ~15 min period of northward IMF and then a second period of southward IMF that lasted for ~45 min. The auroral observations showed an equatorward penetration of the oval by ~3° to Λ ~66° during this period 2. After decreasing substantially during the preceding northward IMF period, there was a very large increase in the midlatitude, subauroral westward flows during period 2. While the flow speeds were similar to those seen during period 1, the flow had far less structuring during period 2, and this difference between the two periods is reflected in the auroral observations.

Convection became very different during the ~4 h time of southward IMF of periods 3 and 4. Very bursty flows were observed, with LOS speeds varying from ~500 m/s to close to 0 m/s repetitively over ~10–20 min periods. The flow bursts had a strong equatorward component and appeared to turn azimuthally as would be expected from a guiding by the large-scale convection pattern. Some of the bursts within the dusk convection cell appear to have penetrated equatorward of the electron plasma sheet, becoming bursts of enhanced flows that were seen in the SAPS region. Auroral streamers were seen throughout the first ~2 h of this period, after which the ASIs with good viewing rotated too far toward the morning section to see streamers. The equatorward boundary of the observed aurora moved rapidly equatorward, from Λ ~66° to Λ ~60°, as seen in the PINA keogram. Based on the radar echo locations and the DMSP electron precipitation observations, the oval continued to expand to Λ ~55° during the first 2 h of this southward IMF interval but did not subsequently expand further.

The above three different modes of electric field occurred following the storm shock and during the storm main phase and were identified using the radar and auroral observations. We have found that the different modes were reflected in the ionospheric and field-aligned current systems. Enhancements of the DP2 and R2 current systems were seen during period 1 and became strongly enhanced during period 2. Similar penetration of the ionospheric currents to midlatitudes was seen during both periods. During periods 3 and 4, when nightside convection consisted of strong bursts with significant spatial structure, both current systems changed from their earlier typical patterns associated with large-scale convection to patterns reflecting the enhanced structure of the electric fields. Also, the currents continued to intensify, the region of strong currents continued to expand equatorward with the auroral oval, and penetrating ionospheric currents continued but with substantial enhanced spatial structure.

The different driving modes were also reflected in the ionospheric densities obtained from vertical TEC measurements. The equatorward boundary of the TEC enhancements, which also represents the poleward boundary of the midlatitude trough, moved equatorward most rapidly after ~07:00 UT, in approximate agreement with what is seen for the auroral oval electron precipitation, the equatorward motion being the most rapid during approximately the first half of period 3. Furthermore, the TEC measurements showed large equatorward moving enhancement features within the auroral oval during periods 3 and 4 of bursty convection; some of which were traceable over ~25–30°of latitude. Simultaneous TEC and radar flow measurements suggest that the TEC enhancements were brought into the auroral oval from the polar cap, and subsequently

moved equatorward and azimuthally within the auroral oval, due to their being carried by the flow bursts as they move from the polar cap to the plasma sheet and then within the plasma sheet.

The earthward injection of particles to form the storm time ring current was found to correspond well with the period of most rapid and furthest equatorward penetration of the auroral oval and associated currents that was associated with bursty convection.

7. Conclusions

In conclusion, during the course of the storm expansion phase, the radar observations indicated the existence of three different southward IMF modes of electric fields that drove storm time phenomena. These three modes were reflected in the aurora and in ionospheric and field-aligned currents. Poleward expansion of auroral oval, which indicates rapid nightside reconnection, occurred primarily during the first driving period, which initiated immediately after the shock impact. Equatorward expansion of the auroral oval occurred predominantly during the period of the third driving mode, when the electric field became extremely bursty with much spatial structure, this structure being reflected by equatorward extending auroral streamers and highly structured ionospheric and field-aligned currents. This also approximately corresponded to the time period of the largest equatorward motion of the ionospheric trough, the biggest earthward injection of ions and electrons into the ring current, and equatorward and azimuthally moving high TEC features within the auroral oval that appear to come from the polar cap. This indicates a common driving of all these storm time features, which are often considered separately. Why the electric field enhancements had these three different manifestations, and why the bursty enhancement interval was more effective in driving storm phenomena, is not clear from our analysis of this one storm. Coordinated and simultaneous multi-instrument observations of main phase phenomena for additional storms would allow for evaluating the generality of the results presented here, and they might also help us understand why certain driving conditions may be more effective than others.

Acknowledgments

Work at UCLA has been supported by NSF grant 1401822 and NASA grants NNX13AD68G and NNX15AF61G. S. Zou is supported by NSF grants AGS1400998 and AGS1342968. SuperDARN is a collection of radars funded by national scientific funding agencies of Australia, Canada, China, France, Japan, South Africa, UK, and United States. J.M.R. acknowledges the support of NSF under award AGS-1341918. The SuperDARN data can be obtained from J.M.R. or viewed using the Virginia Tech SuperDARN website at http://vt.superdarn.org/. S.G.S. acknowledges support from NSF under award AGS-1341925. The DMSP data are maintained by the Air Force Research Laboratory and Applied Physics Laboratory at Johns Hopkins University. CIGO magnetometer data are from the University Alaska magnetometer array. We thank I. R. Mann, D.K. Milling, and the CARISMA for the CARISMA magnetometer data, which is from the University of Alberta and funded by the Canadian Space Agency. OMNI data were downloaded from CDAWeb. We thank the AMPERE team and the AMPERE Science Center for providing the Iridium-derived data products. We thank the SuperMAG, PI Jesper W. Gjerloev for making the SuperMAG indices available at http://supermag.jhuapl.edu/. The Poker Flat

References

Amm, O., and A. Viljanen (1997), Ionospheric elementary current systems in spherical coordinates and their application, *J. Geomagn. Geoelectr.*, *49*(7), 947–955, doi:10.5636/jgg.49.947.

Anderson, B. J., H. Korth, C. L. Waters, D. L. Green, V. G. Merkin, R. J. Barnes, and L. P. Dyrud (2014), Development of large-scale Birkeland currents determined from the Active Magnetosphere and Planetary Electrodynamics Response Experiment, *Geophys. Res. Lett.*, *41*, 3017–3025, doi:10.1002/2014GL059941.

Angelopoulos, V. (2008), The THEMIS mission, *Space Sci. Rev.*, *141*(1–4), 5–34, doi:10.1007/s11214-008-9336-1.

Antonova, E. E. (2006), Stability of the magnetospheric plasma pressure distribution and magnetospheric storms, *Adv. Space Res.*, *38*(8), 1626–1630, doi:10.1016/j.asr.2005.05.005.

Antonova, E. E., and M. V. Stepanova (2015), The problem of the acceleration of electrons of the outer radiation belt and magnetospheric substorms, *Earth Planets Space*, *67*(1), 1–8, doi:10.1186/s40623-015-0319-7.

Baker, D. N., et al. (2014), Gradual diffusion and punctuated phase space density enhancements of highly relativistic electrons: Van Allen Probes observations, *Geophys. Res. Lett.*, *41*, 1351–1358, doi:10.1002/2013GL058942.

Blake, J. B., et al. (2013), The Magnetic Electron Ion Spectrometer, *Space Sci. Rev.*, *179*(1–4), 383–421, doi:10.1007/s11214-013-9991-8.

Boudouridis, A., E. Zesta, R. Lyons, P. C. Anderson, and D. Lummerzheim (2003), Effect of solar wind pressure pulses on the size and strength of the auroral oval, *J. Geophys. Res.*, *108*(A4), 8012, doi:10.1029/2002JA009373. [Available at http://www.agu.org/pubs/crossref/2003/2002JA009373.shtml, accessed 2010-08-15.]

Boudouridis, A., E. Zesta, L. Lyons, P. Anderson, and D. Lummerzheim (2004), Magnetospheric reconnection driven by solar wind pressure fronts, *Ann. Geophys.*, *22*(4), 1367–1378, doi:10.5194/angeo-22-1367-2004.

Boudouridis, A., E. Zesta, L. R. Lyons, P. C. Anderson, and D. Lummerzheim (2005), Enhanced solar wind geoeffectiveness after a sudden increase in dynamic pressure during southward IMF orientation, *J. Geophys. Res.*, *110*, A05214, doi:10.1029/2004JA010704.

Crowley, G. (1996), Critical review of ionospheric patches and blobs, in *Review of Radio Science 1993–1996*, edited by W. R. Stone, chap. 27, pp. 619–648, Oxford Science Publ., U. K.

de la Beaujardière, O., L. R. Lyons, J. M. Ruohoniemi, E. Friis-Christensen, C. Danielsen, F. J. Rich, and P. T. Newell (1994), Quiet-time intensifications along the poleward auroral boundary near midnight, *J. Geophys. Res.*, *99*(A1), 287–298, doi:10.1029/93JA01947.

Gjerloev, J. W. (2012), The SuperMAG data processing technique, *J. Geophys. Res.*, *117*, A09213, doi:10.1029/2012JA017683.

Gkioulidou, M., A. Ukhorskiy, D. G. Mitchell, T. Sotirelis, B. Mauk, and L. J. Lanzerotti (2014), The role of small-scale ion injections in the buildup of Earth's ring current pressure: Van Allen Probes observations of the March 17th, 2013 storm, *J. Geophys. Res. Space Physics*, *119*, 7327–7342, doi:10.1002/2014JA020096.

Hori, T., A. Shinbori, N. Nishitani, T. Kikuchi, S. Fujita, T. Nagatsuma, O. Troshichev, K. Yumoto, A. Moiseyev, and K. Seki (2012), Evolution of negative SI-induced ionospheric flows observed by SuperDARN King Salmon HF radar, *J. Geophys. Res.*, *117*, A12223, doi:10.1029/2012JA018093.

Hudson, M. K., J. Paral, B. T. Kress, M. Wiltberger, D. N. Baker, J. C. Foster, D. L. Turner, and J. R. Wygant (2015), Modeling CME-shock-driven storms in 2012–2013: MHD test particle simulations, *J. Geophys. Res. Space Physics*, *120*, 1168–1181, doi:10.1002/2014JA020833.

Kauristie, K., V. A. Sergeev, O. Amm, M. V. Kubyshkina, J. Jussila, E. Donovan, and K. Liou (2003), Bursty bulk flow intrusion to the inner plasma sheet as inferred from auroral observations, *J. Geophys. Res.*, *108*(A1), 1040, doi:10.1029/2002JA009371.

Incoherent Scatter Radar is operated by SRI International on behalf of the U.S. National Science Foundation under NSF Cooperative Agreement AGS-1133009, and the data are available at http://amisr.com/amisr/links/data-access/. We thank M. Nicholls and M. McCready for their assistance with this radar data. The Van Allen Probes data from EMFISIS were obtained from https://emfisis.physics.uiowa.edu/data/index, the MagEIS data from http://www.rbsp-ect.lanl.gov/data_pub/, and the THEMIS data from http://themis.ssl.berkeley.edu/themis-data/. We acknowledge NASA contract NAS5-02099 for use of data from the THEMIS mission. Specifically, J.W. Bonnell and F.S. Mozer were thanked for the use of EFI data; J.P. McFadden for the use of ESA data; and for the ASI, we thank S. Mende, the CSA for the logistical support in fielding and data retrieval from the GBO stations, and NSF for the support of GIMNAST through grant AGS-1004736. We thank the many different groups operating magnetometer arrays for providing data used in the SECS analysis: (1) AUTUMNX magnetometer network is funded through the Canadian Space Agency/Geospace Observatory Canada program, Athabasca University, Centre for Science/Faculty of Science and Technology, 2014; (2) the Canadian Magnetic Observatory Network is maintained and operated by the Geological Survey of Canada (http://gsc.nrcan.gc.ca/geomag); (3) Geophysical Institute Magnetometer Array is operated by the Geophysical Institute, University of Alaska (more information about this data set is available at http://magnet.asf.alaska.edu/); (4) the Magnetometer Array for Cusp and Cleft Studies array is supported by U.S. National Science Foundation grant ATM-0827903 to Augsburg College; (5) we would like to would like to thank Anna Naemi Willer for calibrating the DTU magnetometers; (6) the McMAC Project is sponsored by the Magnetospheric Physics Program of National Science Foundation and maintained by Peter Chi; (7) the Solar and Terrestrial Physics magnetometer file storage is at the Department of Earth and Planetary Physics, University of Tokyo, and maintained by Kanji Hayashi (hayashi@grl.s.u-tokyo.ac.jp); and (8) the USGS Geomagnetism Program. All data are properly cited and referred to in the reference list or in the acknowledgments.

Kikuchi, T., S. Tsunomura, K. Hashimoto, and K. Nozaki (2001), Field-aligned current effects on midlatitude geomagnetic sudden commencements, *J. Geophys. Res.*, *106*(A8), 15,555–15,565, doi:10.1029/2001JA900030.

Kletzing, C. A., et al. (2013), The Electric and Magnetic Field Instrument Suite and Integrated Science (EMFISIS) on RBSP, *Space Sci. Rev.*, *179*(1–4), 127–181, doi:10.1007/s11214-013-9993-6.

Kurth, W. S., S. De Pascuale, J. B. Faden, C. A. Kletzing, G. B. Hospodarsky, S. Thaller, and J. R. Wygant (2015), Electron densities inferred from plasma wave spectra obtained by the Waves instrument on Van Allen Probes, *J. Geophys. Res. Space Physics*, *120*, 904–914, doi:10.1002/2014JA020857.

Li, W., et al. (2014), Radiation belt electron acceleration by chorus waves during the 17 March 2013 storm, *J. Geophys. Res. Space Physics*, *119*, 4681–4693, doi:10.1002/2014JA019945.

Li, Z., M. Hudson, B. Kress, and J. Paral (2015), Three-dimensional test particle simulation of the 17–18 March 2013 CME shock-driven storm, *Geophys. Res. Lett.*, *42*, 5679–5685, doi:10.1002/2015GL064627.

Lyons, L. R., Y. Nishimura, H.-J. Kim, E. Donovan, V. Angelopoulos, G. Sofko, M. Nicolls, C. Heinselman, J. M. Ruohoniemi, and N. Nishitani (2011), Possible connection of polar cap flows to pre- and post-substorm onset PBIs and streamers, *J. Geophys. Res.*, *116*, A12225, doi:10.1029/2011JA016850.

Lyons, L. R., et al. (2015), Azimuthal flow bursts in the inner plasma sheet and possible connection with SAPS and plasma sheet earthward flow bursts, *J. Geophys. Res. Space Physics*, *120*, 5009–5021, doi:10.1002/2015JA021023.

Mauk, B. H., N. J. Fox, S. G. Kanekal, R. L. Kessel, D. G. Sibeck, and A. Ukhorskiy (2013), Science objectives and rationale for the Radiation Belt Storm Probes mission, *Space Sci. Rev.*, *179*(1–4), 3–27, doi:10.1007/s11214-012-9908-y.

Mende, S. B., S. E. Harris, H. U. Frey, V. Angelopoulos, C. T. Russell, E. Donovan, B. Jackel, M. Greffen, and L. M. Peticolas (2008), The THEMIS array of ground-based observatories for the study of auroral substorms, *Space Sci. Rev.*, *141*(1–4), 357–387, doi:10.1007/s11214-008-9380-x.

Nishimura, Y. et al. (2010), Preonset time sequence of auroral substorms: Coordinated observations by all-sky imagers, satellites, and radars, *J. Geophys. Res.*, *115*, A00I08, doi:10.1029/2010JA015832. [Available at http://www.agu.org/pubs/crossref/2010/2010JA015832.shtml, accessed 2011-03-26.]

Pitkänen, T., A. T. Aikio, and L. Juusola (2013), Observations of polar cap flow channel and plasma sheet flow bursts during substorm expansion, *J. Geophys. Res. Space Physics*, *118*, 774–784, doi:10.1002/jgra.50119.

Rideout, W., and A. Coster (2006), Automated GPS processing for global total electron content data, *GPS Solut.*, *10*(3), 219–228, doi:10.1007/s10291-006-0029-5.

Shi, Y., E. Zesta, L. R. Lyons, J. Yang, A. Boudouridis, Y. S. Ge, J. M. Ruohoniemi, and S. Mende (2012), Two-dimensional ionospheric flow pattern associated with auroral streamers, *J. Geophys. Res.*, *117*, A02208, doi:10.1029/2011JA017110. [Available at http://www.agu.org/pubs/crossref/2012/2011JA017110.shtml, (Accessed 27 March 2012).]

Takahashi, N., Y. Kasaba, A. Shinbori, Y. Nishimura, T. Kikuchi, Y. Ebihara, and T. Nagatsuma (2015), Response of ionospheric electric fields at mid-low latitudes during sudden commencements, *J. Geophys. Res. Space Physics*, *120*, 4849–4862, doi:10.1002/2015JA021309.

Waters, C. L., B. J. Anderson, and K. Liou (2001), Estimation of global field aligned currents using the Iridium® system magnetometer data, *Geophys. Res. Lett.*, *28*(11), 2165–2168, doi:10.1029/2000GL012725.

Weygand, J. M., O. Amm, A. Viljanen, V. Angelopoulos, D. Murr, M. J. Engebretson, H. Gleisner, and I. Mann (2011), Application and validation of the spherical elementary currents systems technique for deriving ionospheric equivalent currents with the North American and Greenland ground magnetometer arrays, *J. Geophys. Res.*, *116*, A03305, doi:10.1029/2010JA016177.

Yu, Y., V. Jordanova, D. Welling, B. Larsen, S. G. Claudepierre, and C. Kletzing (2014), The role of ring current particle injections: Global simulations and Van Allen Probes observations during 17 March 2013 storm, *Geophys. Res. Lett.*, *41*, 1126–1132, doi:10.1002/2014GL059322.

Zesta, E., H. J. Singer, D. Lummerzheim, C. T. Russell, L. R. Lyons, and M. J. Brittnacher (2000), The effect of the January 10, 1997, pressure pulse on the magnetosphere-ionosphere current system, in *Magnetospheric Current Systems*, edited by S.-I. Ohtani, et al., pp. 217–226, AGU, Washington D. C. [Available at http://onlinelibrary.wiley.com/doi/10.1029/GM118p0217/summary, accessed 2016-04-12.]

Zhang, Q.-H., et al. (2013), Direct observations of the evolution of polar cap ionization patches, *Science*, *339*(6127), 1597–1600, doi:10.1126/science.1231487.

Zou, S., L. R. Lyons, M. J. Nicolls, and C. J. Heinselman (2009), PFISR observations of strong azimuthal flow bursts in the ionosphere and their relation to nightside aurora, *J. Atmos. Sol. Terr. Phys.*, *71*(6–7), 729–737, doi:10.1016/j.jastp.2008.06.015.

Zou, S., M. B. Moldwin, A. Coster, L. R. Lyons, and M. J. Nicolls (2011), GPS TEC observations of dynamics of the mid-latitude trough during substorms, *Geophys. Res. Lett.*, *38*, L14109, doi:10.1029/2011GL048178. [Available at http://europa.agu.org/?view=article&uri=/journals/gl/gl1114/2011GL048178/2011GL048178.xml&t=gl,2011,zou, accessed 2011-08-17.]

Zou, Y., Y. Nishimura, L. R. Lyons, E. F. Donovan, J. M. Ruohoniemi, N. Nishitani, and K. A. McWilliams (2014), Statistical relationships between enhanced polar cap flows and PBIs, *J. Geophys. Res. Space Physics*, *119*, 151–162, doi:10.1002/2013JA019269.